Analyzing inflow in a lensed galaxy at z=2.45

Erin Coleman
Department of Physics and Astronomy, University of California, Davis

Understanding the baryon cycle is crucial to forming an accurate picture of the evolution of galaxies, as gas inflows and outflows vary throughout a galaxy's lifetime and affect its star formation rate. At redshift $z \sim 2$, it is highly unusual to observe star-forming galaxies with significant inflow but no outflow component. We present spectroscopic analysis of a galaxy at redshift $z = 2.452$ which exhibits signs of inflow in several ultraviolet ISM absorption lines, and no outflow. The absorption lines are redshifted by $\sim$290 km s^{-1} with respect to the systemic redshift. Modeling stellar continuum features suggests that this galaxy has a low metallicity ($\sim$5% solar) and a very young starburst with age $\sim$4 Myr dominating the ultraviolet luminosity. We conclude that this system is likely in the beginning of a cycle of bursty star formation, where inflow and star formation rates are high, but where supernovae and other feedback processes have yet to become sufficiently strong to launch strong outflow signatures. The gas inflow velocity suggests an approximate halo mass of $\sim 10^{11} M_{\odot}$, a regime in which simulations predict that bursty star formation is common at this redshift. The rarity of observations of redshifted ISM gas absorption is likely due to the short time scale on which these conditions are present in systems undergoing bursty star formation.

1. INTRODUCTION

Galaxy formation is a complex process which is not yet fully understood. The growth of galaxies is driven by gravitational accretion, which provides the gas from which new stars form, and is regulated by outflows of gas driven by star formation and supermassive black hole feedback [1]. These inflow and outflow processes are collectively known as the baryon cycle. All models of galaxy evolution must account for outflow to accord with observational data [e.g., 2].

Gas is ejected through several major mechanisms associated with star formation: radiation pressure, where momentum from photons is transferred to the ambient interstellar medium (ISM); supernovae, when a massive star's core collapses and releases enormous amounts of energy; and stellar winds, which consist of gas being ejected from a star's atmosphere. These processes collectively eject large-scale outflows of gas from galaxies when the star formation density exceeds a threshold of $\gtrsim 0.1$ M$_{\odot}$ yr^{-1} [3].

Rates of inflow, outflow, and star formation vary throughout a galaxy's lifetime. The cosmic star formation density is observed to reach a peak during the period between approximately $z \sim$ 2–3, referred to as "cosmic noon" [4]. At these redshifts, large cosmological accretion rates and high gas fractions within galaxies can result in bursty star formation (i.e., highly time-variable; [5, 6]). Bursty star formation occurs when a large amount of gas is converted into stars on short timescales, which may be driven by accretion or merger events. This star formation and the associated strong outflows deplete the ISM of a galaxy. This has the effect of halting star formation until a sufficient gas reservoir is re-established from inflows. This process is most pronounced in low-mass galaxies, where gas can more easily escape the gravitational potential well. It is also more common at high redshifts [7], where specific accretion rates and gas fractions are higher.

Observationally it is well-established that essentially all star forming galaxies at $z \gtrsim 2$ drive large-scale outflows. The most ubiquitous outflow signature is the blueshift of interstellar absorption lines (and redshift of Lyα emission) relative to a galaxy's systemic velocity [8, 9]. While inflowing gas should also be prevalent, it is much harder to discern, and there are relatively few clear cases of inflow signatures at cosmic noon. Even in cases with redshifted absorption velocities indicating inflows, outflowing gas is also prominent [9].

In this paper, we study the properties of a star-forming galaxy at $z = 2.452$ which shows spectroscopic evidence of inflowing gas, but no outflow. This galaxy is gravitationally lensed by a foreground group at $z = 0.214$, enabling high-quality spectroscopy thanks to the lensing magnification. The lens system was identified in the Cambridge Sloan Survey of Wide Arcs in the Sky (CSWA; this system ID is CSWA 128; [10]) based on a bright multiply imaged arc at $z = 2.225$. The $z = 2.452$ source was first identified using ground based AO imaging by Sharma et al. [11], who estimated a redshift of $z \simeq 2.9$, and is referred to therein as System 10. To maintain clarity and consistency, we will refer to the target $z = 2.452$ galaxy as System 10 throughout this paper.

The structure of this paper is as follows. In Section 2 we discuss the spectroscopic data collection and processing. Section 3 describes our analysis, which includes estimating the systemic redshift by fitting the prominent C IV emission (a strong emission doublet produced by triply ionized carbon) and other features, determining the velocity profile of several interstellar absorption lines relative to the systemic redshift, and modeling the stellar continuum to determine age and metallicity. In Section 4 we discuss our findings in the context of previous observational work and theoretical predictions. Finally, we discuss our conclusions and prospects for future study in Section 5.

2. DATA

CSWA 128 was observed with the Keck Cosmic Web Imager (KCWI; [12]) on 2 June 2019 and 19-20 June 2020 for a total integration time of 8.2 hours. We used the medium slicer and BL grating, providing a 16×20 arcsec field of view with wavlength coverage 3500-5500 Å and spectral resolution 2.4 Å FWHM (R $\simeq$ 1800). Data were taken in orthogonal position angles of 45 and 135 degrees in order to achieve an

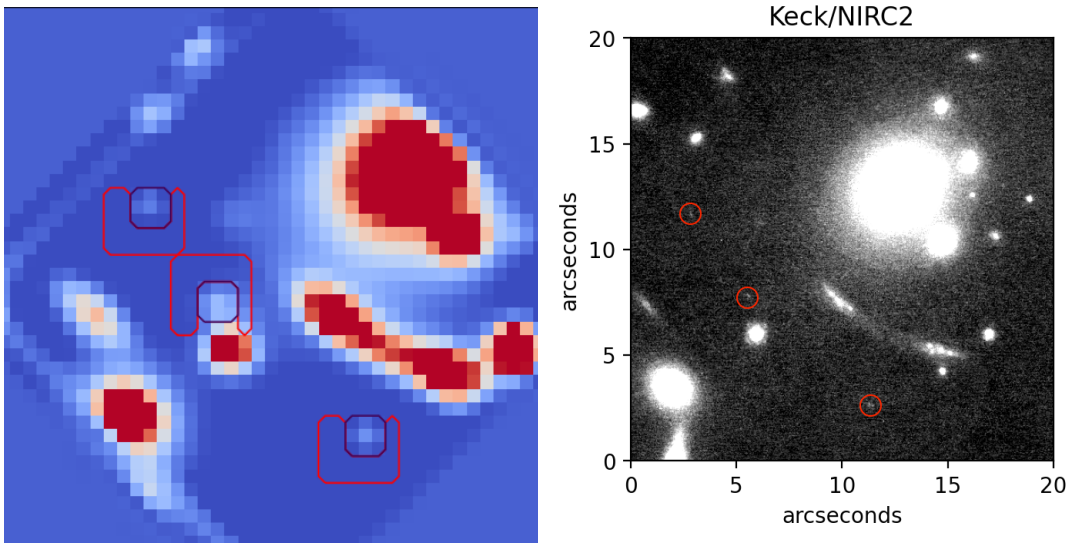

FIG. 1: Images of the CSWA 128 lens system. Both panels are oriented with north up and east to the left. Three magnified images of System 10 are marked in each panel. *Left panel:* White-light optical image obtained by averaging the KCWI datacube used in this work over $\lambda = 3500$–5500 Å. Black outlines show the region used to extract spectra for each image of System 10, and red outlines indicate the regions used to correct sky subtraction residuals around each image. *Right panel:* Keck NIRC2 near-IR adaptive optics image (see [11] for details).

approximately circular point spread function in the combined data cube. Sky conditions were clear to partly cloudy (up to ∼0.5 mag extinction), with FWHM seeing ranging from 0.7–1.25 arcsec. The data were reduced following the procedure described in [13]. In short, we used the KDERP-v1.0.2 pipeline which removes instrument signatures, subtracts background signals from the region of sky being studied, and performs wavelength calibration and spatial rectification, including a correction for differential atmospheric refraction. The reduced datacubes were fit with a 2D first order polynomial to correct for any nonzero residual structure. Individual exposures were then aligned and averaged to produce the final datacube used in this work. Figure 1 shows the white-light image obtained by taking a mean of the reduced datacube over observed wavelengths 3500–5500 Å.

The target of this study is the three lensed images shown in Figure 1, first identified as a multiply imaged galaxy by Sharma et al. [11] based on adaptive optics imaging. From their lens model, this galaxy was estimated to have a redshift of $z = 2.90 \pm 0.25$ [11]. Our KCWI spectra confirm the multiple images with an unambiguous redshift of $z = 2.45$ (Figure 2; Section 3 A). The KCWI datacube is affected by variable sky subtraction residuals, resulting from a dearth of blank sky regions in this lensing group field, with amplitude comparable to the flux of our target. We correct for this residual structure using the average of blank sky spaxels near each of the target image. The reference sky regions are shown in Figure 1. Additional blank sky regions were also used to estimate the uncertainty in our spectra. We subtract the adjacent sky residual from the spectrum of each lensed image of System 10, and confirm that all three images have consistent spectral shapes. We then sum the spectra of all three images to increase the signal-to-noise ratio. The resulting 1-D summed spectrum is shown in Figure 2.

3. ANALYSIS

System 10 exhibits strong C IV $\lambda\lambda$1549, 1551 doublet emission characteristic of young, hot stars [14]. C IV refers to an atomic transition from carbon which has been triply ionized. In general, transitions are referred to by the element and ionization state they occur in, starting by notating neutral atoms with the Roman numeral I. The interstellar absorption components of this C IV feature are clearly redshifted compared to the nebular emission components, which is a robust sign that System 10 is experiencing inflow. All of the well-detected ISM absorption lines are redshifted with respect to the nebular emission redshift, indicating that the absorbing medium has a positive line-of-sight velocity relative to the stars (i.e., inflowing). Of these lines, only the Si II λ1260 shows any significant blueshifted component. As redshifted absorption is unusual in galaxies at this cosmic epoch, we explore the characteristics of this absorption and offer a theoretically-motivated explanation of this phenomenon. In this section, we will detail how we measure the redshift from these lines and quantify the inflowing gas characteristics by modelling the lines and stellar continuum.

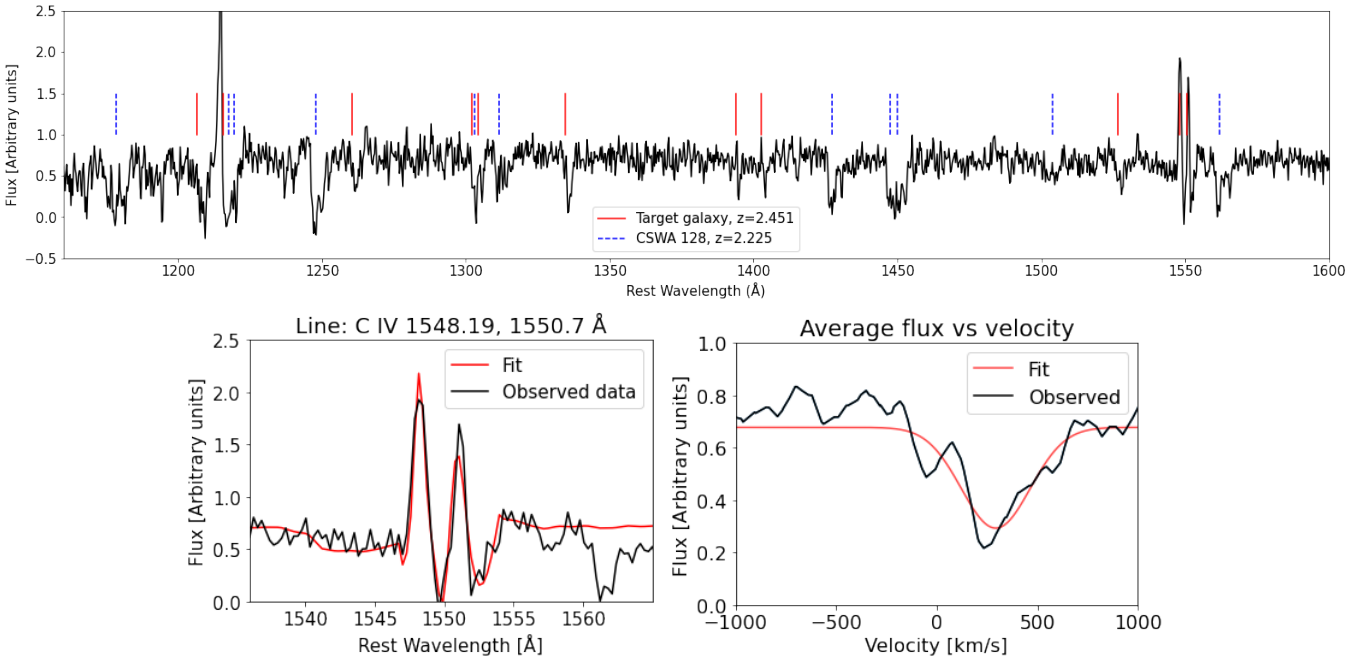

FIG. 2: *Top:* Spectrum of System 10, obtained by summing the three multiple images. Solid red lines indicate strong ISM absorption features at the redshift of System 10, which show signatures of gas inflow. Dashed blue lines indicate intervening absorption features at the redshift $z = 2.225$ of the brighter arc, arising from its circumgalactic medium. Spectral regions affected by intervening absorption are not used in this work. *Bottom left:* Spectrum in the region of C IV . Nebular emission is prominent, with interstellar absorption which is redshifted relative to the emission features, indicative of inflows. The best fit model of the C IV feature is shown in red. *Bottom right:* Average velocity profile of several strong ISM absorption lines with respect to the rest frame of the galaxy. Note that the absorption for negative (blueshifted) velocities is nearly zero.

A. Systemic redshift

We modeled the C IV $\lambda\lambda$1549, 1551 emission and absorption features using a sum of four Gaussian profiles convolved with a Gaussian with FWHM 2.4 Å to account for the line spread function from the spectral resolution of KCWI. We used the scipy `curve_fit` function for all fits discussed in this paper. The model has four free parameters each for the absorption and emission components, representing the amplitude of the λ = 1548.195 Å line, the spread (i.e., Gaussian σ width, corresponding to the distribution of observed redshifts of the feature), the relative amplitude of the 1550.770 Å line compared to the 1548.195 Å line, and the redshift. The values found for each of these parameters are summarized in Table 1.

	Emission	Absorption
Redshift	2.45062 $\pm$ 0.00008	2.4547$\pm$ 0.0002
Amplitude 1549	3.08 $\pm$ 0.59	-1.50 $\pm$ 0.28
Relative amplitude 1551	0.500 $\pm$ 0.096	0.83 $\pm$0.24
Spread (Å)	0.54 $\pm$ 0.11	1.50 $\pm$ 0.24

TABLE 1: Summary of the best fit parameters of the C IV model.

The C IV lines are resonant lines, such that scattering can broaden the emission lines and cause their peaks to shift. In the case of inflowing gas, the emission lines can be scattered to shorter wavelengths. Resonant scattering in the CGM may be less likely for metal-poor, high redshift systems [14], but this effect must be considered. Because the C IV may be scattered, it does not necessarily trace the true systemic redshift.

In an effort to quantify the resonant scattering of the C IV lines, we measured the redshift of Si II*λ 1264 and λ 1533 fine structure transitions, and the emission component of the Si IV λ1939, 1402 features, which can also be good estimates of a galaxy's systemic redshift. This is complicated by the facts that Si IV lines are also resonant, and that the observed redshift of the Si II* lines may be shifted by the spatial distribution of inflowing and outflowing gas. We modeled these four silicon ion emission lines. We fit each Si II* emission independently with a Gaussian profile. The Si IV lines are close in wavelength and emitted by the same ion, so we used a joint fit for both lines following the same procedure as for C IV . Table 2 lists the best-fit redshift for each of these lines.

The measured redshift from the C IV lines is indeed lower than values obtained from the Si lines, as one might expect from resonant scattering. This suggests that the C IV model may underestimate the true systemic redshift by ~ 70 km s^{-1} based on the average of the other lines.

To quantify the resonant scattering of the C IV lines and

Line	Redshift Estimate
Si II* 1264 Å	2.4521 ± 0.0007
Si IV 1393, 1402 Å	2.4514 ± 0.0005
Si II* 1533Å	2.4508 ± 0.0005

TABLE 2: The redshifts found by fitting each of four ionized silicon emission lines present in our data.

Line	$V_{\rm abs}$ relative to $z_{\rm sys}$(km s^{-1})	σ (km s^{-1})
Si II 1260 Å	420± 80	371±100
C II 1334 Å	330±50	170±40
Si IV 1393, 1402 Å	30± 110	130±140
Si II 1526 Å	170±60	220±60

TABLE 3: The velocities relative to $z_{\rm sys}$and velocity dispersions found by fitting each absorption line.

obtain a more accurate estimate of the systemic redshift, we assume that the Si II* lines reflect the true, unscattered redshift, although they have a much lower signal to noise ratio than the C IV lines. We find that the difference between the two Si II* lines detected is 110 ± 70 km s^{-1}, which is consistent with the fact that Si II* lines tend to trace systemic redshift within 50 km s^{-1}. The average velocity of the Si II* lines with respect to the redshift of the C IV lines is 72 ± 38 km s^{-1}, so it is likely that the C IV lines are scattered blueward by 70 km s^{-1}. We adopt the average of the Si II* lines, $z = 2.4515 \pm 0.0004$, as the best estimate of the true systemic redshift for our analysis purposes.

Despite the uncertainty in the precise redshift of System 10, it is abundantly clear that this galaxy has matter inflowing relative to its rest frame and very little outflow because the absorption component of the C IV feature is redshifted relative to the emission component.

B. ISM gas kinematics and dynamical mass

We used the estimate of the systemic redshift found in Section 3 A to calculate the ISM gas velocity relative to the galaxy itself. We examined the strongest ISM absorption lines covered by the KCWI spectra. The spectra cover multiple strong ISM transitions from low- and high-ionization species (See Figure 2). Note that several features in this spectrum, most notably Lyman α at observed wavelength $\lambda \sim 4200$ Å and the Si II λ1302 and O I λ1304 features at observed wavelength $\lambda \sim 4500$ Å are blended with intervening absorption features from the foreground $z = 2.225$ arc. These blended features are not used in the analysis of System 10's properties. The lines available for this analysis were Si II λ1260, C II λ1334, Si II λ1526, and the Si IV λ1393, 1402 doublet.

We modeled these unblended lines, again using a Gaussian convolved with the FWHM 2.4 Å instrument line spread function. Table 3 lists the velocity dispersions and centroids for each line relative to the estimated systemic $z = 2.4515$. Note that Si IV is also a resonant doublet, such that the absorption component may appear more redshifted than the intrinsic inflowing gas.

We also transformed the neighborhood around each line to rest-frame velocity space, and averaged the flux in each neighborhood. We fitted this average spectrum to a Gaussian. The bottom right panel of Figure 2 shows this along with the fit.

We averaged the line velocity profiles to characterize general properties of the inflowing material. By fitting this averaged profile, we found that the absorbing gas has a radial velocity centroid of 290 ± 20 km s^{-1} and a velocity dispersion of $\sigma = 196 \pm 5$ km s^{-1} relative to $z_{\rm sys}$(see Figure 2). We find that the inflowing gas is enriched with heavy metals such as carbon and silicon, which must have originated in a galaxy at some point previously. The gas likely came from this galaxy or is part of an ongoing galaxy merger.

By contrast, Steidel et al. [9], who measured ISM velocity centroids from the rest-frame UV spectra of 89 galaxies at similar $z \sim 2.5$, found little evidence for infalling gas. The expected signature of such gas is a redshifted absorption velocity between 0 and 300 km s^{-1} with respect to the systemic velocity, and with line profiles reversed with respect to those they found for outflowing gas [9]. This galaxy shows precisely these signatures, as seen in Figure 3. From the redshifts of several ISM absorption lines, we estimate that gas is entering this galaxy at a velocity of 293±20 km sec^{-1}. The velocity profile is reversed from those found by [9], with the highest absorption at the redshifted end of the profile.

To determine whether the velocity found is compatible with gravitationally-driven inflow, we also studied the mass of the galaxy. In Appendix A, we calculate the velocity gained by an object falling towards the galactic center from the virial radius as a function of halo mass. We use a standard NFW model for the density of a dark matter halo. We find that a velocity of 293 km sec^{-1} is consistent with a dark matter halo of mass of approximately $10^{11} M_{\odot}$. This is on the low end for the samples of galaxies at cosmic noon studied by [15] [9], but is a reasonable estimate.

The baryonic mass of a galaxy is a small fraction of the total dynamical mass (with baryons making up an average of approximately 10% of the total mass [15] [16]), but like the total dynamical mass, can also give an estimate of the galaxy's relative size. A halo mass of $10^{11} M_{\odot}$ corresponds to a stellar mass of approximately $10^8 - 10^9 M_{\odot}$ [17]. The baryonic mass is related to the galaxy's velocity dispersion σ by the relation

$$M_{dyn} = C\sigma^2 r/G, \tag{1}$$

where C may vary between 1 and 5 depending on the distribution of mass within in a galaxy [15]. Although the precise value of C may vary, this relationship means that the velocity dispersion is an important metric related to the galaxy's mass. We calculate the velocity dispersion of the emission lines to be 34 ± 6 km sec^{-1}. This is one of the lowest velocity dispersions found in a survey of 110 galaxies at cosmic noon presented by [15]. This galaxy's emission shows a very low velocity dispersion compared to other galaxies at similar redshifts, which suggests that it is low in mass [15] [9].

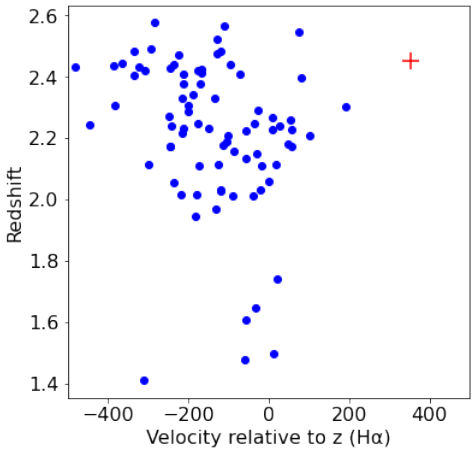

FIG. 3: A plot of the redshift vs ISM absorption line velocities of a sample of galaxies at redshift $z \sim 2$. Blue circles represent the sample of galaxies studied in [9][15], while the red cross represents System 10. System 10 shows a clear inflow, in contrast to the Steidel sample, which all have negative or near-zero velocities.

C. Modeling stellar populations

We compared the observed stellar continuum with Binary Population and Spectral Synthesis (BPASS) v2.2 [18] models of varying stellar ages and metallicities. These models take an initial mass function (IMF), an age, and a metallicity and output the intensity of light emitted at each wavelength by the corresponding population of stars. The initial mass function determines the number of stars of various masses at the beginning, before the system evolves over the time period given. In this case, we used `imf135_300`, corresponding to the Salpeter IMF [19] with an upper mass cutoff of 300 $M_\odot$, which is considered to be standard by the creators of BPASS.

We fit the models to the observed spectra in several wavelength ranges which are sensitive to the stellar age and metallicity. The ranges used correspond to the stellar wind features C IV $\lambda\lambda$1549, 1551 and Si IV $\lambda\lambda$1394, 1403, and between rest-frame $1350 - 1390$ Å which contains photospheric absorption features and anchors the continuum level. These regions were chosen to avoid strong interstellar absorption and emission lines, which BPASS does not model. Accordingly the wavelengths with narrow emission and ISM absorption in C IV and Si IV were not used in the fit. We corrected for the effects of dust reddening by scaling the models with a power-law function in wavelength, λ^β, which gives a reasonable approximation and good match to the data over the relatively narrow wavelength range considered here. The stellar P-Cygni wind features are highly constraining, whereas we do not resolve individual photospheric lines at the spectral resolution of the KCWI data. Our data show weak stellar winds (Figure 2), which suggests a low metallicity [14]. From a χ^2 analysis we find that the best-fit model has a metallicity $Z = 0.001$ (5% of the solar value) and age of 4.0 Myr. This is comparable to results from studies of strong C IV emitters at $z \sim 0$. In particular, Senchyna et al. [14] found that galaxies with strong C IV nebular emission have ultraviolet spectra dominated by stars between 3 and 22 Myr old, with metallicities below 10% solar.

4. DISCUSSION

This galaxy's absorption profile, indicating gas inflows and no outflows, is highly unusual compared to previously studied star forming galaxies of similar redshift. The rarity of this observational signature suggest that the conditions which create it are short lived. An intriguing possibility is that we may be witnessing the onset of a bursty star formation episode in this galaxy. Cosmological simulations suggest galaxies of all masses at cosmic noon tend to be undergoing a starburst less than 20% of the time, with the fraction of stellar mass formed in starbursts decreasing with increasing galaxy mass. In simulations of low mass galaxies ($M_\star \lesssim 10^9 M_\odot$), nearly all stars may be formed during starbursts [5]. Such simulations show a time sequence whereby gas inflow triggers star formation, and subsequently stellar feedback drives outflows, which remove the gas and cause star formation to cease [7]. In this scenario, we expect to see signatures of inflow and no outflow for only a few million years at the beginning of a starburst before the stellar feedback begins to take effect. In a starburst that lasts 50 Myr, this phase might last only 25 Myr. If a galaxy undergoes starbursts less than 20% of the time [7], this suggests that this type of signature might be present in around 10% of galaxies of this mass, metallicity, and age.

Our BPASS modeling further suggests that this is a low-mass galaxy seen shortly after the onset of a starburst. We find that the ultraviolet emission is dominated by metal-poor stars (suggesting a low stellar mass; [20]) with an age of only ∼4 Myr. Our dynamical measurements in Section 3 B also suggest a low mass. Simulations suggest that starburst durations can range from ∼ 3-50 Myr [5], compatible with our best-fit age. At 4 Myr, many massive stars have yet to go supernova.

Stellar winds, although strongest in massive young stars, are weaker for metal-poor stars and indeed we see relatively weak stellar P-Cygni features in our target. Radiation pressure also couples more strongly to metallic elements, leading to less transfer of momentum in a low metallicity galaxy. The combination of these three factors could lead to weak outflows, allowing absorption signatures to be dominated by inflowing material.

The galaxy size is also quite small, including in near-IR adaptive optics imaging, which is more sensitive to older stellar populations because older stars emit longer wavelength light (Figure 1). A possibility is that outflows may be occurring in a direction away from the line of sight (i.e., in a location not directly between the star forming regions and the observer). Such geometric effects can be particularly strong in compact galaxies such as this one. Outflowing gas not directly in front of the star forming region would not be observable in absorption signatures, as no starlight would shine through it.

These explanations do not explain the dearth of observations of inflow in other high redshift galaxies. Inflow frequently occurs in streams, while outflow is more spherically symmetric, meaning that line of sight effects are more relevant for inflow. However, in lower redshift galaxies ($0 < z < 1$), where outflows are still common [21], there are still observations of galaxies dominated by inflow [22]. However, observations of higher redshift galaxies do not show any with significant inflow in the interstellar lines.

The data support the hypothesis that this profile is the result of bursty star formation in a galaxy with a low metallicity and low mass. FIRE simulations suggest that bursty star formation is most common in young, low mass galaxies with low metallicity at high redshifts [11].

5. CONCLUSIONS

In this work, we presented spectroscopic measurements of a galaxy at redshift $z = 2.4505$, magnified by strong gravitational lensing. Analysis of the nebular emission and several absorption lines prevalent in the interstellar medium reveal an unambiguous signature of inflowing gas travelling with a radial velocity around 290 ± 20 km s^{-1}. We propose that bursty star formation, as well as potential effects of compactness and the line-of-sight viewing angle, may be responsible for the strong inflow and lack of outflow signature in the interstellar UV absorption lines.

The majority of ISM velocity measurements available at cosmic noon are in much more massive galaxies, which are expected to be less bursty, i.e. with more continuous star formation which drives continuous outflows. Galaxies with a stellar mass of $M_* = 10^{10} M_\odot$ spend less than half of their time in burst cycles [5]. As discussed previously, the mass of System 10, as implied by emission line width and metallicity, is much lower than many other samples. Simulations predict very bursty star formation for galaxies with stellar mass below approximately $10^{10} M_\odot$, but samples frequently contain few to zero galaxies of that mass [15], [9].

This is the first galaxy at redshift $z \sim 2$ observed to have inflow and no outflow, and is one of a small number of low-mass observed galaxies at high redshift. Cosmological simulations (such as FIRE) find that these inflowing states are short-lived, which partly explains the rarity of this observational signature. The burstiness required to fuel this type of pattern is uncommon in higher mass galaxies, which make up the majority of spectroscopic observations at cosmic noon. If a survey of young, low-mass galaxies at cosmic noon were to be conducted, we predict that approximately 10% might show a similar absorption profile. Although intrinsically faint, the combination of strong gravitational lensing and high redshift rest-UV spectroscopy offers a promising approach to study the nature of bursty star formation and the baryon cycle in low-mass galaxy formation.

Acknowledgements

I would like to thank my mentor this summer, Tucker Jones. Many thanks to Keerthi Vasan G.C., Yuguang Chen, and other group members for their advice and support. Finally, I would like to thank the NSF's physics REU at the University of California, Davis for providing funding for this research under grant PHY-2150515.

This research has made use of the Keck Observatory Archive (KOA), which is operated by the W. M. Keck Observatory and the NASA Exoplanet Science Institute (NExScI), under contract with the National Aeronautics and Space Administration. The data presented herein were obtained at the W. M. Keck Observatory, which is operated as a scientific partnership among the California Institute of Technology, the University of California and the National Aeronautics and Space Administration. The Observatory was made possible by the generous financial support of the W. M. Keck Foundation. The authors wish to recognize and acknowledge the very significant cultural role and reverence that the summit of Maunakea has always had within the indigenous Hawaiian community. We are most fortunate to have the opportunity to conduct observations from this mountain.

[1] Jason Tumlinson, Molly S. Peeples, and Jessica K. Werk. The Circumgalactic Medium. , 55(1):389–432, August 2017.

[2] Rachel S. Somerville and Romeel Davé. Physical Models of Galaxy Formation in a Cosmological Framework. , 53:51–113, August 2015.

[3] T. M. Heckman. Galactic Superwinds at Low and High Redshift. In John E. Hibbard, Michael Rupen, and Jacqueline H. van Gorkom, editors, *Gas and Galaxy Evolution*, volume 240 of *Astronomical Society of the Pacific Conference Series*, page 345, January 2001.

[4] Piero Madau and Mark Dickinson. Cosmic Star-Formation History. , 52:415–486, August 2014.

[5] Martin Sparre, Christopher C. Hayward, Robert Feldmann, Claude-André Faucher-Giguère, Alexander L. Muratov, Dušan Kereš, and Philip F. Hopkins. (Star)bursts of FIRE: observational signatures of bursty star formation in galaxies. *Monthly Notices of the Royal Astronomical Society*, 466(1):88–104, April 2017. arXiv:1510.03869 [astro-ph].

[6] Hakim Atek, Jean-Paul Kneib, Camilla Pacifici, Matthew Malkan, Stephane Charlot, Janice Lee, Alejandro Bedregal, Andrew J. Bunker, James W. Colbert, Alan Dressler, Nimish Hathi, Matthew Lehnert, Crystal L. Martin, Patrick McCarthy, Marc Rafelski, Nathaniel Ross, Brian Siana, and Harry I. Teplitz. Hubble Space Telescope Grism Spectroscopy of Extreme Starbursts across Cosmic Time: The Role of Dwarf Galaxies in the Star Formation History of the Universe. *Astrophys. J.* , 789(2):96, July 2014.

[7] Alexander L. Muratov, Dusan Keres, Claude-Andre Faucher-Giguere, Philip F. Hopkins, Eliot Quataert, and Norman Murray. Gusty, gaseous flows of FIRE: galactic winds in cosmological simulations with explicit stellar feedback. *Monthly Notices of the Royal Astronomical Society*, 454(3):2691–2713, December 2015. arXiv:1501.03155 [astro-ph].

[8] Alice E. Shapley, Charles C. Steidel, Max Pettini, and Kurt L. Adelberger. Rest-Frame Ultraviolet Spectra of z˜3 Lyman Break Galaxies. *Astrophys. J.* , 588(1):65–89, May 2003.

[9] C. C. Steidel, D. K. Erb, A. E. Shapley, M. Pettini, N. A. Reddy, M. Bogosavljević, G. C. Rudie, and O. Rakic. The Structure and Kinematics of the Circum-Galactic Medium from Far-UV Spectra of z˜2-3 Galaxies. *The Astrophysical Journal*, 717(1):289–322, July 2010. arXiv:1003.0679 [astro-ph].

[10] Daniel P. Stark, Matthew Auger, Vasily Belokurov, Tucker Jones, Brant Robertson, Richard S. Ellis, David J. Sand, Alexei Moiseev, Will Eagle, and Thomas Myers. The CASSOWARY spectroscopy survey: a new sample of gravitationally lensed galaxies in SDSS. *Monthly Notices of the Royal Astronomical Society*, 436(2):1040–1056, December 2013.

[11] Soniya Sharma, Johan Richard, Tiantian Yuan, Anshu Gupta, Lisa Kewley, Vera Patrício, Nicha Leethochawalit, and Tucker A. Jones. High Resolution spatial analysis of a z $\sim$ 2 lensed galaxy using adaptive coadded source-plane reconstruction. *Monthly Notices of the Royal Astronomical Society*, 481(2):1427–1440, December 2018. arXiv:1808.10468 [astro-ph].

[12] Patrick Morrissey, Matuesz Matuszewski, D. Christopher Martin, James D. Neill, Harland Epps, Jason Fucik, Bob Weber, Behnam Darvish, Sean Adkins, Steve Allen, Randy Bartos, Justin Belicki, Jerry Cabak, Shawn Callahan, Dave Cowley, Marty Crabill, Willian Deich, Alex Delecroix, Greg Doppman, David Hilyard, Ean James, Steve Kaye, Michael Kokorowski, Shui Kwok, Kyle Lanclos, Steve Milner, Anna Moore, Donal O'Sullivan, Prachi Parihar, Sam Park, Andrew Phillips, Luca Rizzi, Constance Rockosi, Hector Rodriguez, Yves Salaun, Kirk Seaman, David Sheikh, Jason Weiss, and Ray Zarzaca. The Keck Cosmic Web Imager Integral Field Spectrograph. *The Astrophysical Journal*, 864(1):93, September 2018. arXiv:1807.10356 [astro-ph].

[13] Kris Mortensen, Keerthi Vasan G. C, Tucker Jones, Claude-André Faucher-Giguère, Ryan L. Sanders, Richard S. Ellis, Nicha Leethochawalit, and Daniel P. Stark. Kinematics of the Circumgalactic Medium of a z = 0.77 Galaxy from Mg ii Tomography. *The Astrophysical Journal*, 914(2):92, June 2021. Publisher: The American Astronomical Society.

[14] Peter Senchyna, Daniel P. Stark, Stephane Charlot, Adele Plat, Jacopo Chevallard, Zuyi Chen, Tucker Jones, Ryan L. Sanders, Gwen C. Rudie, Thomas J. Cooper, and Gustavo Bruzual. Direct Constraints on the Extremely Metal-Poor Massive Stars Underlying Nebular C IV Emission from Ultra-Deep HST/COS Ultraviolet Spectroscopy. *The Astrophysical Journal*, 930(2):105, May 2022. arXiv:2111.11508 [astro-ph].

[15] Dawn K. Erb, Charles C. Steidel, Alice E. Shapley, Max Pettini, Naveen A. Reddy, and Kurt L. Adelberger. The Stellar, Gas and Dynamical Masses of Star-Forming Galaxies at z˜2. *The Astrophysical Journal*, 646(1):107–132, July 2006. arXiv:astro-ph/0604041.

[16] S. Giodini, D. Pierini, A. Finoguenov, G. W. Pratt, H. Boehringer, A. Leauthaud, L. Guzzo, H. Aussel, M. Bolzonella, P. Capak, M. Elvis, G. Hasinger, O. Ilbert, J. S. Kartaltepe, A. M. Koekemoer, S. J. Lilly, R. Massey, H. J. McCracken, J. Rhodes, M. Salvato, D. B. Sanders, N. Z. Scoville, S. Sasaki, V. Smolcic, Y. Taniguchi, D. Thompson, and the COSMOS collaboration. SLAR AND TOTAL BARYON MASS FRACTIONS IN GROUPS AND CLUSTERS SINCE REDSHIFT 1*. *The Astrophysical Journal*, 703(1):982, September 2009. Publisher: The American Astronomical Society.

[17] Peter S. Behroozi, Risa H. Wechsler, and Charlie Conroy. The Average Star Formation Histories of Galaxies in Dark Matter Halos from z = 0-8. *The Astrophysical Journal*, 770:57, June 2013. ADS Bibcode: 2013ApJ...770...57B.

[18] E R Stanway and J J Eldridge. Re-evaluating old stellar populations. *Monthly Notices of the Royal Astronomical Society*, 479(1):75–93, September 2018.

[19] Edwin E. Salpeter. The Luminosity Function and Stellar Evolution. *Astrophys. J.* , 121:161, January 1955.

[20] Ryan L. Sanders, Alice E. Shapley, Mariska Kriek, Naveen A. Reddy, William R. Freeman, Alison L. Coil, Brian Siana, Bahram Mobasher, Irene Shivaei, Sedona H. Price, and Laura de Groot. The MOSDEF Survey: Mass, Metallicity, and Star-formation Rate at z ˜2.3. *Astrophys. J.* , 799(2):138, February 2015.

[21] Kate H. R. Rubin, J. Xavier Prochaska, David C. Koo, Andrew C. Phillips, Crystal L. Martin, and Lucas O. Winstrom. EVIDENCE FOR UBIQUITOUS COLLIMATED GALACTIC-SCALE OUTFLOWS ALONG THE STAR-FORMING SEQUENCE AT z 0.5. *The Astrophysical Journal*, 794(2):156, October 2014. Publisher: The American Astronomical Society.

[22] G W Roberts-Borsani and A Saintonge. The prevalence and properties of cold gas inflows and outflows around galaxies in the local Universe. *Monthly Notices of the Royal Astronomical Society*, 482(3):4111–4145, January 2019.

[23] Julio F Navarro, Carlos S Frenk, and Simon D M White. The Structure of Cold Dark Matter Halos.

[24] Anatoly Klypin, Gustavo Yepes, Stefan Gottlober, Francisco Prada, and Steffen Hess. MultiDark simulations: the story of dark matter halo concentrations and density profiles. *Monthly Notices of the Royal Astronomical Society*, 457(4):4340–4359, April 2016. arXiv:1411.4001 [astro-ph].

Appendix A: Halo mass calculations

We will calculate the velocity of gas falling inward from the virial radius under the influence of gravity as a function of halo mass to determine whether the inflow velocity measured is plausible. The inflowing gas we observe is metal-enriched, so it is likely being recycled within the halo, as gas from the IGM would have much lower heavy element content. Thus, we want to consider gas falling from a radius less than or equal to the virial radius. Approximating the galaxy's dark matter halo as an isotropic sphere, we approximated the mass density of the dark matter halo of System 10 using NFW density profiles [23], with the form

$$\rho_{\rm NFW}(r) = \frac{\rho_0}{xC(xC+1)^2}, x \equiv \frac{r}{R_{vir}}. \quad \text{(A1)}$$

The variable R_{vir} is the virial radius, which is the radius inside which a gravitationally bound system, such as a galaxy, obeys the virial theorem $\langle T \rangle = -\frac{1}{2}\langle U \rangle$. The virial radius is typically used as a cutoff for the extent of a dark matter halo. The other parameters, ρ_0 and C, represent the mass density at a critical radius r_{-2} and the concentration of the halo, or the location of that critical radius, $C = \frac{R_{vir}}{r_{-2}}$. NFW mass density profiles are a standard model for the density of a galaxy's dark matter halo. Although these profiles can deviate from the true halo profile of a galaxy, these deviations are small for low mass galaxies like this one [24].

The concentration is a function of the total mass, and we used the following concentration-mass relation and parameters provided by [24]:

$$C(M) = C_0 \left(\frac{M}{10^12 h^{-1} M_\odot}\right)^{-\gamma} \left[1 + \left(\frac{M}{M_0}\right)^{0.4}\right] \quad \text{(A2)}$$

with parameters $C_0 = 2.42$, $\gamma = 0.080$, and $M_0 = 1.7 \times 10^{13} h^{-1} M_\odot$. These parameters correspond to a Planck cosmology with redshift of 2.5. The halo density profile is then determined by a single free parameter ρ_0, which maps to the total dark matter halo mass. Under this model, a halo of $10^{11} M_\odot$, as suggested by the inflow velocity, has a concentration of approximately 3.3.

By calculating the change in gravitational potential of an object falling from the virial radius to the center, we can calculate the change in velocity experienced by such an object. This free-fall velocity increases with total halo mass as shown in Figure 4. According to this model, the 290 km s^{-1}inflow velocity we observe is consistent with a total halo mass between 10^{10} and $10^{11} M_\odot$.

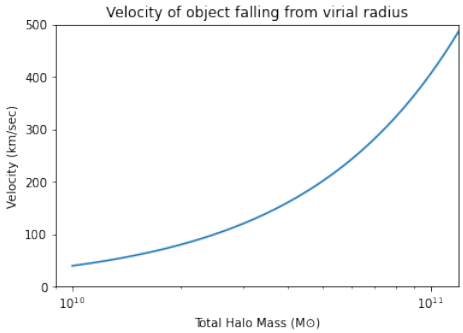

FIG. 4: The change in velocity of an object at rest falling from the virial radius of a galaxy to the center of a dark matter halo as a function of total halo mass.